

Structure and Observational Properties of Supercritical Accretion Discs with Optically-Thick Outflows

P. ABOLMASOV¹, S. KARPOV¹

and

Taro KOTANI²

¹*Special Astrophysical Observatory, Nizhnij Arkhyz 369167, Russia*

²*Dept. of Physics, Tokyo Tech, 2-12-1 O-okayama, Tokyo 152-8551*

pasha@sao.ru

(Received ; accepted)

Abstract

Highly supercritical accretion discs are probable sources of dense optically-thick axisymmetric winds. We introduce a new approach based on diffusion-approximation radiative transfer in a funnel geometry and obtain an analytical solution for the energy density distribution inside the wind assuming that all the mass, momentum and energy are injected well inside the spherization radius. This allows to derive the spectrum of emergent emission for various inclination angles. We show that self-irradiation effects play an important role altering the temperature of the outcoming radiation by about 20% and the apparent X-ray luminosity by a factor of $2 \div 3$. The best-fit parameters of the model applied to several ULXs may be briefly characterized as moderate ejection rates $\dot{m} \sim 10^2$ and small half-opening angles $\theta_f \sim 5 \div 10^\circ$. The basic properties of the high ionization HII-regions found around some of ULXs are also easily reproduced in our assumptions.

Key words: Physical Data and Processes: diffusion, accretion, accretion discs
X-rays: individual (SS433, ULXs)

1. Introduction

Processes of gas accretion onto compact objects are studied since 60s when first X-ray sources were discovered (Frank et al. 2002). Among several works describing the details of disc accretion in binary systems Shakura & Sunyaev (1973) was the most successfull. Their “standard disc” is still widely used to describe the thermal component of X-ray spectra of X-ray binaries. Standard disc model was worked out in several considerations such as high optical thickness, low geometrical thickness of the disc, etc. Among these assumptions one was that the power released in the accretion process does not exceed the Eddington luminosity and does not

therefore influence the dynamics of the flow. This case is usually called subcritical accretion.

However, considering various phenomena such as growth of supermassive black holes and nova outbursts leads to the problem of supercritical accretion. It has been extensively investigated since 1980s when Abramowicz proposed it as a power source for active galactic nuclei (Abramowicz et al. 1980). Presently super-Eddington accretion is often applied to explain the observational properties of Ultraluminous X-ray Sources (ULXs, see Roberts (2007) for observational review) that are believed to be high-mass X-ray binaries with black holes accreting on thermal time scale.

The first, outflow-dominated model of supercritical accretion, has been developed by Shakura and Sunyaev in the paper mentioned above. Authors assumed that all the inflowing gas above the critical accretion rate is being ejected from the disc in the form of a wind. Another version of supercritical regime is based on the relaxation of the locality condition in “standard model” which leads to advective slim discs (Abramowicz et al. 1980) or Polish doughnuts (Abramowicz 2004). In reality, both processes work simultaneously.

A comprehensive model taking into account both for advection and ejection was recently developed by Poutanen et al. (2007). Authors consider the structure of the disc in radial direction and estimate three characteristic temperatures relevant for the outcoming radiation (inner disc temperature, temperature at spherisation radius and effective temperature of the wind photosphere) but do not study the processes of radiation transfer in the wind and do not calculate the outcoming spectra.

Obviously, at high accretion rates the observational properties of the accretion flow are governed mostly by radiative transfer in the outflowing wind. Currently, we have at least one example of a persistent supercritical accretor (SA) in our Galaxy – the SS433 system, where most of accreting gas is being lost in a wind.

Numerical simulations of this system partially support the outflow-dominated scenario. However, Okuda (2002) states that his thorough 2D simulation fails to reproduce the outflow rate and jet collimation in SS433. In Ohsuga et al. (2005) a supercritical accretor (SA) accreting at 10^3 Eddington rate appears a bright (about 10^{38} ergs $^{-1}$) hard X-ray source if viewed edge-on. Ohsuga et al. (2005) and Heinzeller et al. (2007) calculate the structure and emergent spectra considering only the inner parts of the flow ($R \leq 500R_G$) not taking into account that the region considered is coated by accreting and outflowing matter both being optically thick. The outcoming spectra will strikingly differ from those calculated by Heinzeller et al. (2007).

Optical and radio (Blundell et al. 2001) observations allow to measure the mass ejection rate in the relatively slow accretion disc wind seen in optical emission and absorption lines (Fabrika 2004) as well as the mass loss rate in the collimated mildly-relativistic jets launched along the disc axis. Infrared excess was used by Shklovskii (1981) and Van den Heuvel (1981) to estimate the mass ejection rate from SS433. No direct mass transfer rate measurements were ever made though it is usually supposed that it could not be much higher than the mass

ejection rate $\dot{M}_{ej} \sim 10^{-4} M_{\odot} \text{yr}^{-1}$ (Fabrika 2004).

The details of the processes in the supercritical disc itself are unclear mainly due to the strong absorption in the wind. In fact even the photosphere of the wind is difficult to study due to high interstellar absorption (about 8^m) making it impossible with the contemporary instrumentation to trace the Spectral Energy Distribution (SED) in the far UV spectral range where most of the radiation is expected to be emitted. The only and yet crude estimate of the blackbody temperature of SS433 was made by Dolan et al. (1997) and probably corresponds to the photosphere of the wind. Their measurements are consistent with a $(2 \div 7) \times 10^4 \text{ K}$ blackbody source.

Both observations of SS433 (Fabrika 2004) and numerical simulations (Okuda 2002; Ohsuga et al. 2005) support the conception that is traditionally called “supercritical funnel”. It assumes that nearly all the matter accreted is being ejected in a form of a slow, roughly virial at spherization radius, dense wind. Due to centrifugal barrier two conical avoidance sectors with half-opening angles of $\theta_f \sim 30^\circ$ are formed along the accretion disc symmetry axis, filled with rarefied hot gas, which may be accelerated and collimated to form relativistic jets (Eggum et al. 1988). In the inner parts of the wind this gas also can form a pseudo-photosphere (“funnel bottom”) at $R_{in} \sim 10^9 \text{ cm}$ (Fabrika 2004). This radius is calculated in the consideration all the material ejected in the relativistic jets is uniformly distributed with respect to the polar angle. In case of any inhomogeneity of the jet material the inner radius becomes lower.

Another class of objects supposed to be supercritical accretors are extragalactic Ultraluminous X-ray sources (ULXs). Katz (1986) supposed that an object similar to SS433 seen at low inclination angles can appear a bright X-ray source with super-Eddington apparent luminosity. ULXs were discovered about that time by *Einstein* (see Fabbiano (1989) and references therein). Though the nature of these sources remains unclear they are good candidates for the objects predicted by Katz (Poutanen et al. 2007).

The question about how representative is SS433 among the SA systems in the observed Universe is difficult to answer. If one considers mass transfer in thermal timescale in a black hole high mass X-ray binary (BHMXB), the most relevant is the mass of the secondary that determines the timescale and hence the scaling for the mass accretion rate. It may be shown that in assumption the radius of the secondary scales with its mass as $R \propto M^{1/2}$ and the black hole mass is close to $10 M_{\odot}$ dimensionless thermal-timescale mass transfer rate depends on the secondary mass as:

$$\dot{m} \simeq \left(\frac{M_2}{M_{\odot}} \right)^{5/2}.$$

For the case of SS433 ($M_2 \simeq 20 M_{\odot}$) our estimate predicts $\dot{m} \sim 2000$, similar to the observed value ¹. If the donor star is highly evolved, accretion rate is higher and less stable and

¹ Actually, there are no direct measurements of the mass transfer rate for SS433. However, the observed

the phase itself is shorter. Unfortunately, initial binary mass ratio distribution for massive stars is poorly known but there are indications that mass ratios close to 1 are much more probable (Lucy 2008; Kobulnicky & Fryer 2007). The thermal timescale mass transfer rates in BHHMXBs are therefore likely to be highly supercritical, $\dot{m} \sim 100 \div 10^4$. Lower yet supercritical rates may take place in case of wind accretion for example in WR+BH binaries (Bauer & Brandt 2004). Those are likely to form a certain sub-sample of evolved ULXs with moderately supercritical accretion rates.

The paper is organized as follows. In the next section we construct a simple analytical model describing the internal structure of an optically-thick wind flow that is likely to develop in the case of very high mass ejection (and accretion) rate \dot{m} . Section 3 is devoted to effects of self-irradiation that are likely to play very important role in our funnel solution. In section 4 we consider the emergent SEDs for arbitrary inclination taking into account self-occultation effects. In section 5 we test it for two sets of publicly available X-ray data. We discuss the implications of the model and its early testing in section 6.

2. Structure of Supercritical Disc Winds

In this section we study the spatial structure of the radiation density field inside the wind. We will use the following set of assumptions (their reliability will be discussed below in Section 6): *(i)* the flow is axisymmetric (also symmetrical with respect to the disc plane) and stationary, *(ii)* the flow is optically thick to true absorption, *(iii)* the velocity and density fields are not affected by energy and entropy transfer (i. e. we consider the wind already accelerated or accelerating/decelerating with a given power-law dependence on radius), *(iv)* all the motions are purely radial and non-relativistic, *(v)* the inner surface of the funnel and spherical photosphere are considered locally blackbody sources and *(vi)* for certainty we suggest the temperature of the bottom equal to the starting temperature of the walls. We simplified the picture somehow suggesting the mass is loaded in the center of symmetry. This assumption is violated in the inner parts of the wind.

We assume that fraction $K \lesssim 1$ of the accreting mass is ejected in the wind. Because mass ejection rate is more relevant (see below) we will use the dimensionless notation $\dot{m} = \dot{M}/\dot{M}_{cr}$ for the **mass ejection rate** where

$$\dot{M}_{cr} = \frac{48\pi GM}{c\kappa_T} \simeq 3 \times 10^{-7} M_{10} \text{ M}_{\odot} \text{ yr}^{-1} \quad (1)$$

is the critical Eddington accretion rate as introduced by Poutanen et al. (2007). M_{10} here is the accretor mass in $10M_{\odot}$ units. Mass accretion is characterised by $\dot{m}/K \sim \dot{m}$, we assume $K = 1$ everywhere below bearing in mind that $K < 1$ results in a hotter and more luminous source but requires higher accretion rate. The outcoming spectra depend mostly on the mass ejection rate.

stability of the orbital period and evolution-time considerations exclude significantly higher mass transfer rates (Fabrika 2004; Goranskij et al. 1998).

Mass accretion rate affects only the luminosity injected at the inner boundary in a logarithmic way. To achieve a 50% change in luminosity (and about 12% change in temperature) for $\dot{m} = 100$ one should assume 90% of the accreting material accreted by the black hole ($K = 0.1$).

There are physical differences between the regime of highly supercritical accretion that we consider here and moderately supercritical accretion ($\dot{m} \sim 1 \div 10$). At $\dot{m} \sim 10$ the flow becomes translucent and relativistic and some of our approximations are violated.

For radial coordinate normalization we will use the “spherization” radius

$$R_{sph} = \frac{3\dot{M}\kappa}{\Omega_f c} = \frac{18}{\cos\theta_f} R_g \dot{m}. \quad (2)$$

This value is proportional to the spherisation radii used by Shakura & Sunyaev (1973)

$$R_{sph}^{(SS)} = \frac{3\dot{M}\kappa}{8\pi c} \quad (3)$$

and by Poutanen et al. (2007)

$$R_{sph}^{(P)} = 5/3\dot{m}, \quad (4)$$

but has also non-trivial dependence on geometry. Normalized radial coordinates will be hereafter denoted by small letters r in contrast to capital R reserved for physical distances.

We assume fixed geometry for the wind funnel, i.e. fixed half-opening angle θ_f independent of the accretion/ejection rate. Note the difference with funnels in Polish doughnuts (Abramowicz 2004) where

$$\theta_f \propto \sqrt{r_{in}/r_{out}} \propto e^{-0.5L/L_{Edd}} \propto \dot{m}^{-0.3}, \quad (5)$$

defined by equipotential surfaces. In contrast, when the wind is launched from a thin but supercritical disk at a certain radius and its velocity in the frame comoving with the disk is $v = \xi v_K$, where v_K is the Keplerian velocity, and normal to the disk surface, the half-opening angle will be a function of ξ only (Poutanen et al. 2007):

$$\theta_f = \arctg \left(1/\sqrt{\xi^2 - 1} \right). \quad (6)$$

Radial velocity of the wind may be uniform ($v = const$) in the case of large initial speed or virial ($v \propto R^{-1/2}$) in the parabolic case when the initial velocity is close to the escape velocity from the wind acceleration region. We adopt a generalized self-similar scaling

$$v = \frac{1}{6\sqrt{\cos\theta_f}} c \dot{m}^{-1/2} r^\alpha \quad (7)$$

with approximately virial value at the spherization radius.

Outside the spherization radius the gas density in the wind scales as

$$n \propto r^{-(2+\alpha)} \quad (8)$$

and vanishes (or, at least, drops by several orders of magnitude) inside the funnel. Inside the spherisation radius deviations from this law are expected and mass ejection rate should depend

on radius roughly as $\dot{m}_{eff} \propto r$, and hence

$$n \propto r^{(-1+\alpha)}. \quad (9)$$

We briefly analyse the consequences of this difference in density slope in section 6.

2.1. Diffusion Equation

The main equation governing energy transfer may be derived from the energy conservation and Fick's laws for the thermal energy flux

$$\mathbf{q} = -D\nabla u, \quad (10)$$

where $D = c/(3\kappa\rho)$ is the diffusion coefficient and u is energy density. The first law of thermodynamics

$$d\left(\frac{u}{n}\right) = Tds + \frac{p}{n^2}dn \quad (11)$$

$$du = nTds + \frac{p+u}{n}dn \quad (12)$$

where

$$Tds = (\nabla \mathbf{q})dt \quad (13)$$

$$du/dt = \partial_t u + (\mathbf{v}\nabla)u \quad (14)$$

$$dn/dt = -n(\nabla \mathbf{v}) \quad (15)$$

may be rewritten in the generic form

$$\partial_t u + (\mathbf{v}\nabla)u - \nabla(D\nabla u) - \gamma u(\nabla \mathbf{v}) = 0 \quad (16)$$

If the specific heat ratio γ does not depend heavily on other parameters, this may be rewritten for an axisymmetric system in terms of enthalpy density $h = \gamma u$ as

$$\begin{aligned} \frac{1}{v}\partial_t u + \partial_r u - \frac{1}{r^{2+\alpha}}\partial_r(r^{4+\alpha}\partial_r u) - \\ - \left(L_\theta - \frac{\gamma(2+\alpha)}{r}\right)u = 0 \end{aligned} \quad (17)$$

where

$$L_\theta = \frac{1}{\sin\theta}\partial_\theta(\sin\theta\partial_\theta) \quad (18)$$

is the polar part of the Laplace operator, and the second term in brackets accounts for adiabatic losses. Equation (17) is linear hence one may separate the variables. Eigenfunctions will depend on $\cos\theta$ as linear combinations of Legendre polynomials P_k and Legendre functions of the second kind Q_k (Jahnke & Emde 1960).

In the stationary case

$$u_k = (P_k(\cos\theta) + a_k Q_k(\cos\theta)) R_k(r) \quad (19)$$

where R_k is the solution of the equation

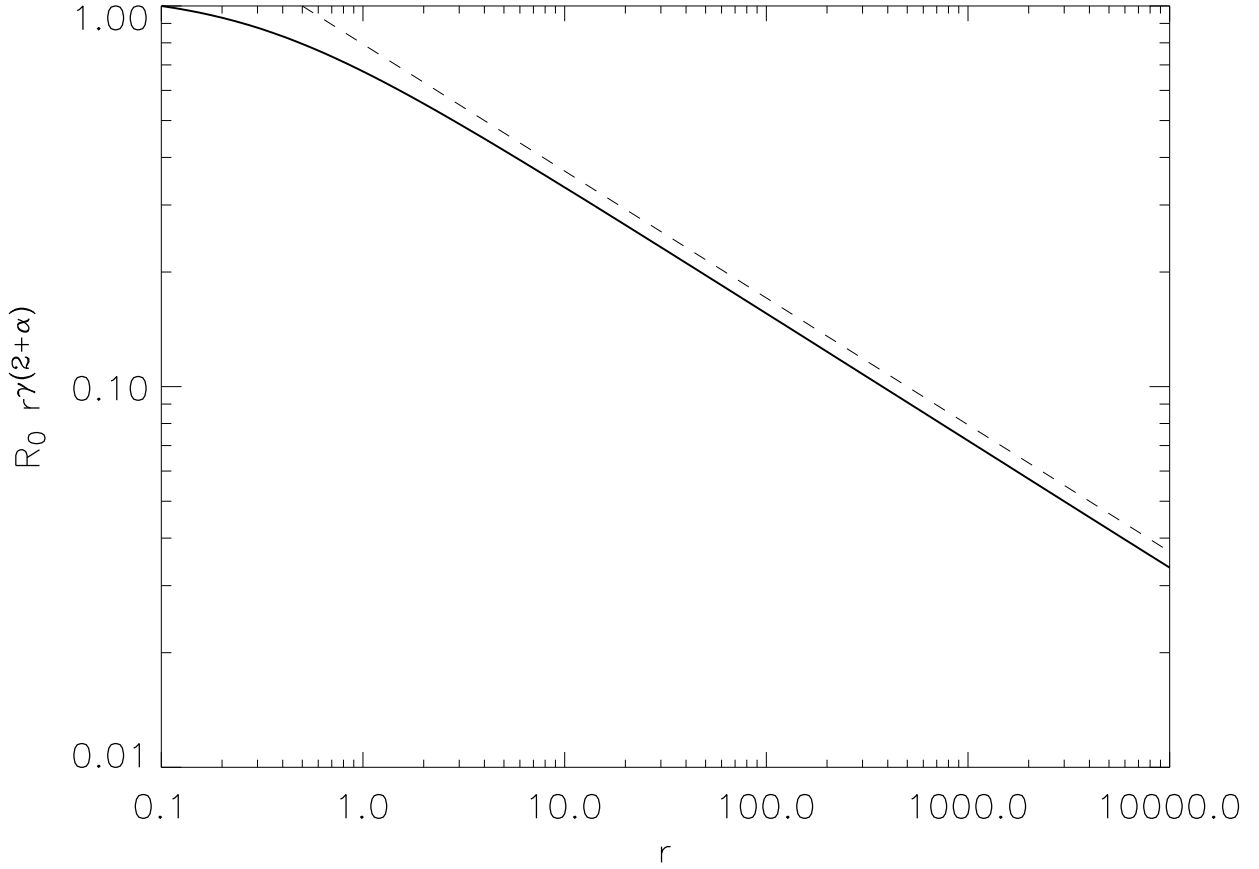


Fig. 1. Radial dependence for the zeroth-order solution for $\alpha = 0$ and $\gamma = 4/3$ (solid line) normalized by the low- r asymptotics. High- r power-law asymptotics $u \propto r^{-(2+\alpha)}$ is shown by a dashed curve.

$$-\frac{1}{r^{2+\alpha}}e^{-1/r}\partial_r\left(r^{4+\alpha}e^{1/r}\partial_ru\right)-\left(k(k+1)-\frac{\gamma(2+\alpha)}{r}\right)u=0 \quad (20)$$

For the zeroth-order ($k=0$) solution asymptotics may be derived both for large distances $r \gg 1$ where diffusion dominates, $e^{-1/r} \simeq 1$ and $u \propto r^{-(3+\alpha)}$, and for very low radii where adiabatic losses prevail and $u \propto r^{-\gamma(2+\alpha)}$. Figure 1 shows the exact numerical solution for the radial eigenfunction R_0 for $\alpha=0$ and $\gamma=4/3$. It may be rather well (with accuracy better than 2%) approximated by the following function

$$Y(r) = \left(1 - e^{-\frac{1}{2+\alpha}\frac{1}{r}}\right)^{1-(\gamma-1)(2+\alpha)} r^{-\gamma(2+\alpha)} \quad (21)$$

2.2. Boundary Conditions

For a system with equatorial plane symmetry the solution will contain only even eigenfunctions. If we choose the inner radius R_{in} well below the spherization radius, equation (20) becomes a first-order one, and is governed by a single parameter which we assume to be the

initial energy density. The latter may be estimated from the total central source luminosity L for the advective flow as

$$u_{in} \sim \frac{L}{\Omega R_{in}^2 v(r_{in}) Y(r_{in})} \quad (22)$$

Luminosity of a supercritical disk in different models depends logarithmically on the dimensionless mass accretion rate (Poutanen et al. 2007; Shakura & Sunyaev 1973) as

$$\begin{aligned} L &= L_{Edd} (1 + 0.6 \ln(\dot{m}/K)) \simeq \\ &\simeq 1.5 \times 10^{39} \frac{1.7}{1+X} M_{10} (2.8 + 0.6 \ln \dot{m}_3) \text{ ergs}^{-1}, \end{aligned} \quad (23)$$

where \dot{m}_3 is the mass ejection rate in $10^3 \dot{M}_{cr}$, X is hydrogen mass fraction in the accreting gas, M_{10} is the accretor mass in $10 M_\odot$ units. Temperature of the flow at the spherization radius is $T \sim 0.1 \dot{m}_3^{-3/8}$ keV while gas density is $n \sim 4 \times 10^{16} \dot{m}_3^{-1/2}$, which leads to a rather high radiation to gas pressure ratio:

$$\beta \simeq \frac{aT^3}{n} \simeq 500 \dot{m}_3^{-5/8} \quad (24)$$

For accretion rates that appear during thermal-timescale mass transfer $10 < \dot{m} < 10^5$ (see also sections 1 and 6) radiation pressure dominates in the advective inner parts of the wind. That allows to equate $\gamma = 4/3$ anywhere in the flow because the wind is radiation-pressure dominated in the regions where γ is relevant.

Energy flux is directed radially in the inner advective parts of the wind and is practically normal to the walls near the funnel wall surface in the outer parts. In figure 2 we present the two-dimensional distribution of energy density and energy flux vector field for our solution. The exact angular dependence of the energy influx at the inner boundary is not very important as it is mixed near the spherization radius, so we will restrict ourselves to a zeroth-order solution.

Funnel wall cools efficiently therefore a simple boundary condition

$$u(r, \theta_f) = 0 \quad (25)$$

may be adopted. The following zeroth-order solution satisfies it and decays fast enough at infinity to account for the photon escape through the funnel walls

$$u = u_0 \cdot \ln \left(\frac{1 - \cos \theta}{1 - \cos \theta_f} \cdot \frac{1 + \cos \theta_f}{1 + \cos \theta} \right) Y(r) \quad (26)$$

u_0 normalization may be derived from the total luminosity (more accurately than in (22)) of the disk as

$$u_0 \simeq \frac{L}{\Omega' R_{in}^2 v(r_{in}) Y(r_{in})} \quad (27)$$

Here we define $\Omega' = -8\pi \ln \sin \theta_f$. $Y(r_{in}) \simeq r_{in}^{-\gamma(2+\alpha)}$ for $r_{in} \ll 1$.

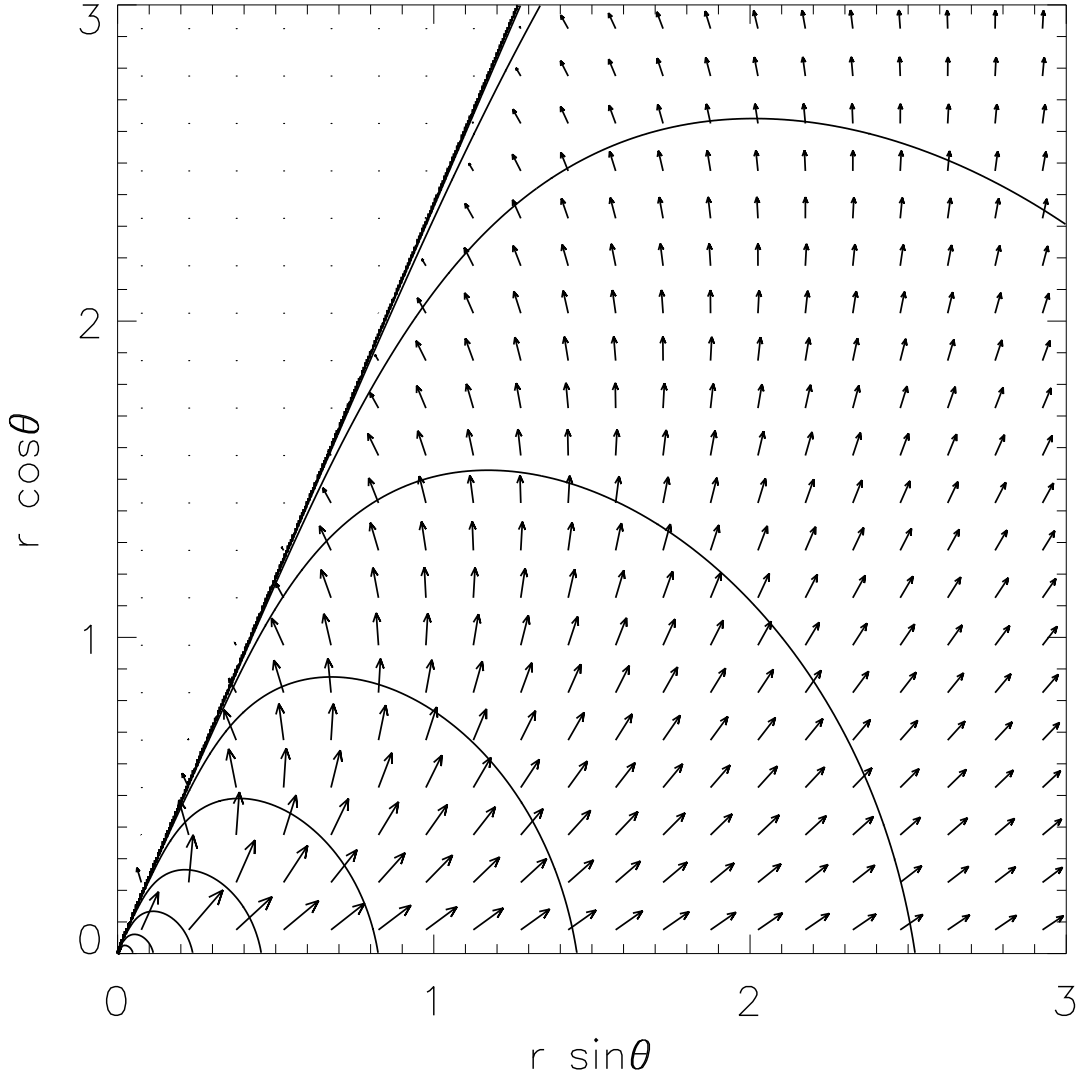


Fig. 2. Two-dimensional distribution of energy density in the optically-thick wind. $\theta_f = 0.4 \simeq 23^\circ$, $\alpha = 0$. Inner funnel wall is shown by a thick solid line. Arrows are oriented in the energy flux direction, their length proportional to the energy flux logarithm.

2.3. Surface Effective Temperature Distribution

Below we consider funnel walls, bottom and outer photosphere blackbody sources with the temperature determined by the normal component of energy flux:

$$F_n = \sigma_B T^4. \quad (28)$$

For the funnel walls it is equal to the latitudal component:

$$F_\theta = \frac{2L}{\Omega' \sin^2 \theta_f R_{sph}^2} \frac{1}{r_{in}^{2+\alpha} Y(r_{in})} r^{1+\alpha} Y(r), \quad (29)$$

and in the case of outer photosphere

$$F_r = -D \partial_r u = \frac{(3+\alpha)L}{\Omega' R_{sph}^2} \frac{1}{r_{in}^{2+\alpha} Y(r_{in})} r^{1+\alpha} Y(r) \cdot \ln \left(\frac{1-\cos \theta}{1-\cos \theta_f} \cdot \frac{1+\cos \theta_f}{1+\cos \theta} \right). \quad (30)$$

Here $r = r_{out}$ should be substituted for the outer photosphere.

Note that the fluxes are of the same order and their ratio does not depend on the radial coordinate.

For the funnel walls one obtains:

$$T_{wall} = 0.038 \left(\Omega' \tan^2 \theta_f r_{in}^{2+\alpha} Y(r_{in}) \right)^{-1/4} \dot{m}_3^{-1/2} M_{10}^{-1/4} (r^{1+\alpha} Y(r))^{1/4} \text{ keV} \quad (31)$$

where M_{10} is the mass of the accretor in $10 M_\odot$ units. Effective temperature scales with radius as

$$T_{wall} \propto r^{-5/12} \quad (32)$$

at lower radii and as

$$T_{wall} \propto r^{-1/2} \quad (33)$$

in the outer parts of the funnel. Temperature slope depends very weakly on all the parameters and is similar to the value $p = 1/2$ (if $T \propto r^{-p}$) characteristic for slim discs (Abramowicz 2004) and supercritical accretion discs with massive outflows. p -free multi-blackbody spectra are characterised by a power-law intermediate asymptotics with photon index $\Gamma = 2/p - 2$. Many ULXs have power-law spectra with $\Gamma \simeq 2$ close to the expected in all these models. The similarity makes it very difficult to distinguish between the various supercritical accretion disc models by their X-ray spectra only.

We assume the temperature of the funnel bottom equal to the effective temperature of the adjacent wall surface

$$T_{bot} = 0.038 \left(\Omega' \tan^2 \theta_f r_{in} \right)^{-1/4} \dot{m}_3^{-1/2} M_{10}^{-1/4} \text{ keV} \quad (34)$$

Minimal inner radius R_{in} may be estimated as the last stable orbit radius divided by $\cos \theta_f$ as $r_{in} = 1/6 \dot{m}$ in R_{sph} units. Temperatures characteristic for the high-energy cut-offs in ULX spectra are about one keV and require $r_{in} \gtrsim \dot{m}^{-1}$. It is clear that in the framework of our

model the inner parts of the funnel should be practically transparent. If we make another assumption that the soft excess in ULX spectra corresponds to $T \sim 0.1 \div 0.2$ keV temperature at the spherisation radius than accretion rates required are $\dot{m} \sim 100$. In section 5 we fit real X-ray spectra with our model obtaining similar results ($r_{in} \sim 10^{-3}$ and $\dot{m} \sim 100$) for two ULXs.

Effective temperature of the photosphere may be found in a similar way. The outer photosphere radius may be estimated as

$$r_{out} \simeq \left(\frac{2\Omega' \sqrt{\dot{m}}}{(1+\alpha) \sqrt{\cos \theta_f}} \right)^{1/(1+\alpha)} \quad (35)$$

in R_{sph} units. The photosphere is significantly non-plane-parallel, but its luminosity and spectral energy distribution may be roughly estimated as:

$$L_{ph} \simeq \frac{(3+\alpha)(2+\alpha)^{(2+\alpha)(\gamma-1)-1}}{r_{in}^{2+\alpha} Y(r_{in})} \cos^2 \theta_f L \quad (36)$$

$$T_{ph} \simeq 0.0048 f_\alpha \left(r_{in}^{2+\alpha} Y(r_{in}) \right)^{-1/4} \sqrt{\cos \theta_f} M_{10}^{-1/4} \dot{m}_3^{-3/4(1+\alpha)} \left(\ln \left(\frac{1-\cos \theta}{1-\cos \theta_f} \cdot \frac{1+\cos \theta_f}{1+\cos \theta} \right) \right)^{1/4} \text{ keV}, \quad (37)$$

where

$$f_\alpha = (3(1+\alpha))^{1/2(1+\alpha)} (2+\alpha)^{((2+\alpha)(\gamma-1)-1)/4} \times (\Omega')^{-(3+\alpha)/4(1+\alpha)}.$$

Characteristic temperatures derived above are fairly consistent with those reported by Poutanen et al. (2007). For a reasonably high $\dot{m} = 10^3$ and $\theta_f = 0.4$ the outer photosphere temperature is about $\sim 10^5$ K. Together with a photospheric luminosity $\sim 10^{39}$ ergs $^{-1}$ this makes the wind photosphere both a bright UV/optical and a bright EUV source capable for ionizing large amounts of interstellar and circumstellar gas. We discuss the properties of HII-regions created by SA wind photospheres in section 6.3. Very shallow temperature decline makes the spectrum flat from $E \sim 0.005$ keV to ~ 1 keV. The highest temperature value is predicted by accretion disc theory and is much higher than the temperature at spherisation radius (Poutanen et al. 2007):

$$T_{max} = 1.27 M_{10}^{-1/4} \text{ keV}. \quad (38)$$

3. Effects of Irradiation

In the standard disc model irradiation is a minor, often negligible effect as the disc is thin and the fraction of emitted luminosity absorbed by the outer parts of the disc is of order of $O(H/R)^2$. On the contrary, in the case of supercritical funnel most of the radiation emitted at any point on the wall surface will be absorbed again or reflected. The probability of re-absorption is of the order of the wind solid angle $\Omega_f = \cos \theta_f$, hence the energy balance of the outer parts of the supercritical funnel surface will be affected by the radiation of the inner

regions. As long as true absorption dominates over electron scattering, $\sigma \gg \sigma_T$, all the quanta may be considered absorbed and re-emitted by the walls remaining a locally blackbody source.

The energy input due to incident radiation is characterized by the flux $F'(R)$ normal to the wall surface and directed inward, which may originate both from the funnel bottom and inner parts of the walls. In general, the incident flux may be expressed as

$$F' = F \int \left(\frac{T_{eff}(\mathbf{R}')}{T_{eff}(\mathbf{R})} \right)^4 \frac{|(\mathbf{n} \cdot \mathbf{d})(\mathbf{n}' \cdot \mathbf{d})|}{d^2} dS' \quad (39)$$

where the meaning of \mathbf{n} and \mathbf{d} vectors is illustrated in figure 3 for both wall and bottom irradiation.

3.1. Problem Formulation

In this section Cartesian and spherical coordinates are used. z axis coincides with the symmetry axis of the disc, funnel and jets. The remaining degree of freedom is adjusted to set to zero the azimuthal coordinate of the point under consideration, where the incident flux is calculated. This point is set by a radius vector \mathbf{R} ,

$$\mathbf{R} = R \begin{pmatrix} \sin \theta \\ 0 \\ \cos \theta \end{pmatrix}$$

In the same way in the following subsections we define the bottom radius vector \mathbf{R}_0 and the radius vector \mathbf{R}' of the variable point on the funnel walls.

$$\mathbf{R}_0 = R_0 \begin{pmatrix} 0 \\ 0 \\ \cos \theta \end{pmatrix} \quad \mathbf{R}' = R' \begin{pmatrix} \sin \theta \cos \varphi \\ \sin \theta \sin \varphi \\ \cos \theta \end{pmatrix}$$

The geometry of funnel self-irradiation is shown in figure 3. Variable infinitesimal plate with area dS' , radius vector \mathbf{R}' and normal \mathbf{n}' contributes to the incident flux in the current point by:

$$dF' = |(\mathbf{n} \cdot \mathbf{d})(\mathbf{n}' \cdot \mathbf{d})| \frac{dS'}{2\pi d^4},$$

where $\mathbf{d} = \mathbf{R}' - \mathbf{R}$, $d = |\mathbf{d}|$. Due to surface brightness invariance from distance it is convinient to use dilution factor w depending on geometry only and to normalize the incident flux over the outcoming flux $F(\mathbf{R})$ in the current point.

$$w = \frac{|(\mathbf{n} \cdot \mathbf{d})(\mathbf{n}' \cdot \mathbf{d})|}{d^2}$$

Incident flux in the units of the outcoming integral flux ($f = F'/F$) can be expressed as an integral over the funnel inner surface:

$$f = \int \left(\frac{\tau(\mathbf{R}')}{\tau(\mathbf{R})} \right)^4 \frac{|(\mathbf{n} \cdot \mathbf{d})(\mathbf{n}' \cdot \mathbf{d})|}{d^2} dS' \quad (40)$$

τ is the local effective temperature in the units of starting (bottom) temperature T_0 . In the case of the funnel bottom we avoid integration suggesting the bottom a point-like source emitting as a flat plate.

3.2. Irradiation by the Funnel Bottom

The first heating term is simpler to handle because the source is practically point-like and its temperature is not affected by the funnel walls. Due to this, one can do without integration. Funnel bottom can be considered a spherical surface with the surface area $S_{sph} = 2\pi(1 - \cos\theta)R_0^2$ or a flat circular plate of radius $R_0 \sin\theta$ (because R_0 is the starting radial coordinate along the wall, not along the z -axis) with the surface area $S = \pi R_0^2 \sin^2\theta$. Both expressions give similar results when $\theta \ll 1$. Here we assume the bottom having flat surface (see figure 3a). The photon source coordinate and normal unit vector are:

$$\mathbf{R}_0 = R_0 \begin{pmatrix} 0 \\ 0 \\ \cos\theta \end{pmatrix} \quad \mathbf{n}_0 = \begin{pmatrix} 0 \\ 0 \\ 1 \end{pmatrix}$$

Distance vector connecting emitting and receiving points:

$$\mathbf{d} = \mathbf{R} - \mathbf{R}_0 = R_0 \begin{pmatrix} r \sin\theta \\ 0 \\ (r - 1) \cos\theta \end{pmatrix}$$

Here $r = R/R_0$. Dilution factor in that case:

$$\begin{aligned} w(x, \theta, \varphi) &= \frac{|(\mathbf{n} \cdot \mathbf{d})(\mathbf{n}_0 \cdot \mathbf{d})|S}{2\pi d^4} = \\ &= \frac{(r-1) \sin\theta \cos^2\theta}{2(1+r^2-2r\cos\theta)^2} \end{aligned} \quad (41)$$

Total normalized irradiating flux from the bottom can be therefore expressed as:

$$f_{bottom} = \frac{1}{2} \frac{(r-1) \sin^3\theta \cos^2\theta}{(1+r^2-2r\cos\theta)^2} T^{-4} \quad (42)$$

3.3. Self-Irradiation by the Funnel Walls

The energy input from the absorbed photons is directly calculated using equation (39). Surface element is an elementary area on a conical surface, $dS' = 2\pi \sin\theta R' dR' d\varphi$. Radius vectors and normals are defined. Distance vector:

$$\mathbf{d} = \mathbf{R}' - \mathbf{R} = R \begin{pmatrix} \sin\theta(1 - x \cos\varphi) \\ -x \sin\theta \sin\varphi \\ \cos\theta(1 - x) \end{pmatrix}$$

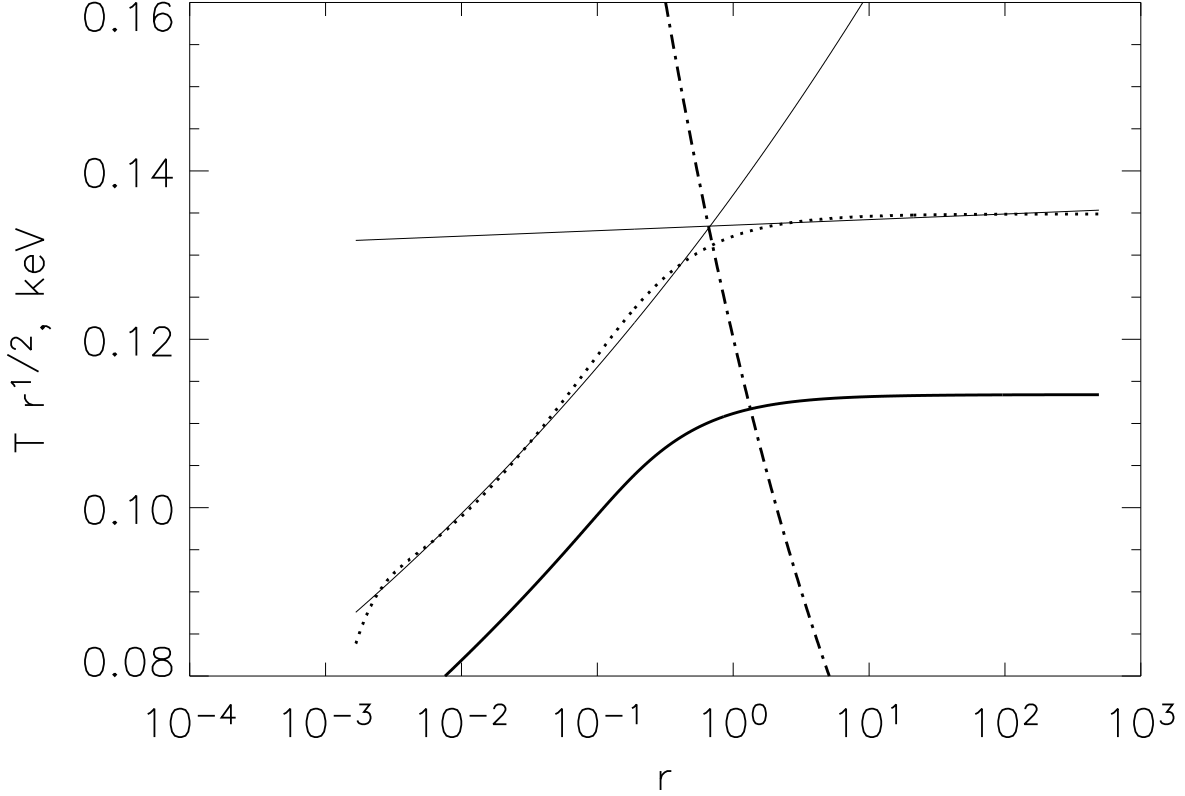


Fig. 4. Funnel wall temperature dependence on radius, normalized by $r^{-1/2}$. Thick solid line: without irradiation, thick dotted line: with irradiation effects. Thin solid lines represent the best power-law fits to the irradiated funnel wall temperature at larger r (> 1) and lower r (< 1), $T \propto r^{-0.43}$ and $T \propto r^{-0.50}$, correspondingly. Dot-dashed line represents the $T \propto r^{-3/4}$ temperature slope characteristic for standard discs.

visible surfaces applying visibility conditions. The most important effect is that at inclinations $i \gtrsim \theta_f$ funnel bottom and some part of the funnel walls become obscured from the observer.

In figures 4 and 5 we compare the temperature profiles and SEDs with and without irradiation. We adopt $\alpha = 0$, $\dot{m} = 10^2$, $r_{in} = 1/6\dot{m} = 1.7 \times 10^{-3}$, $\theta_f = 23^\circ$. The temperature dependence on radius is close to a broken power-law in both cases, and the net effect of irradiation is in altering the mean temperature at any given radius by about 20%. In figure 5 SEDs are calculated for zero inclination. Two components, funnel (X-rays and hard EUV) and photosphere radiation (UV and optical), may be seen in the SEDs. Evidently, only the funnel component is affected by irradiation that alters the flux by a factor of $2 \div 3$. Spectrum is practically flat in the EUV/soft X-ray region but curves near the $T_{sph} \sim 0.1$ keV. High-energy cut-off is present at several keV if the inner radius is $r_{in} \sim 1/\dot{m}$.

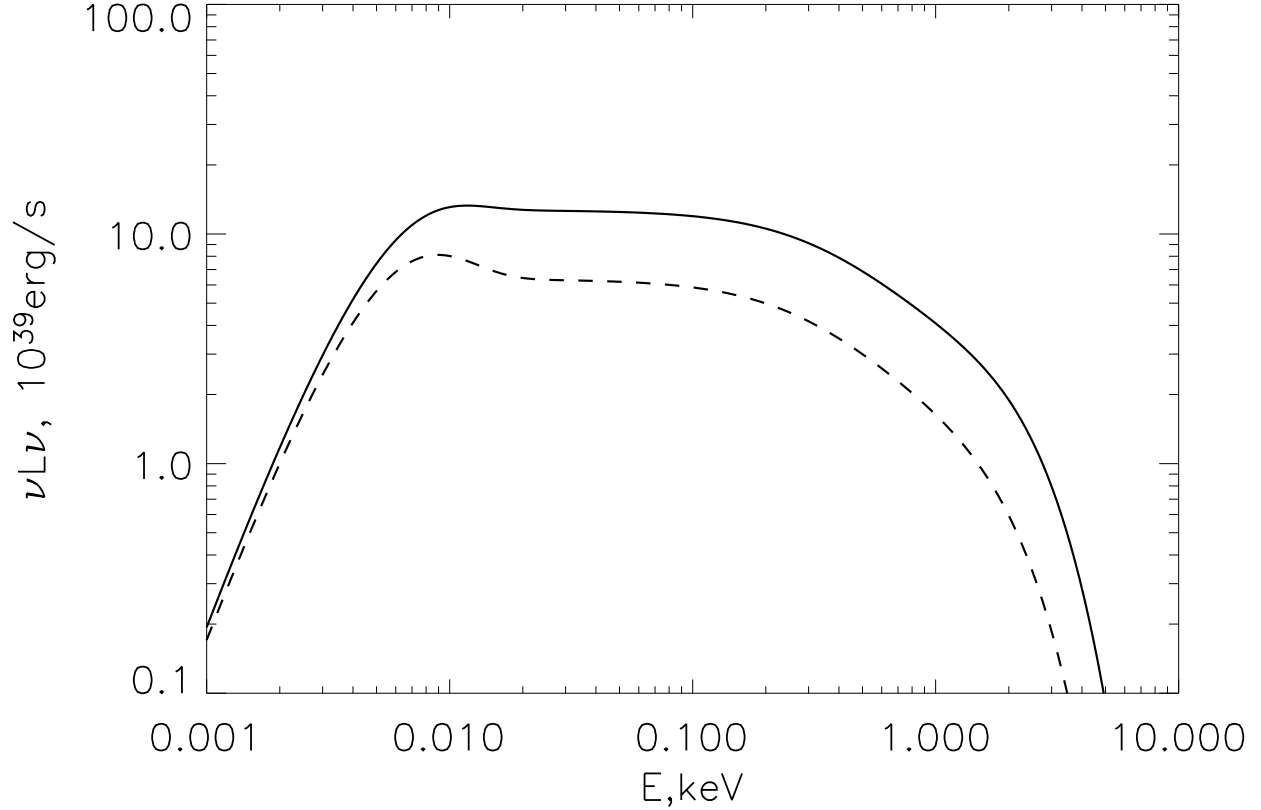


Fig. 5. Irradiation effects on the outcoming spectrum. Dashed line corresponds to the face-on spectrum calculated using a simple analytical model (section 2) and the solid line takes into account irradiation effects. Parameters are the same as in the previous figure.

4.1. Self-Occultation

Let i be the inclination of the funnel (angle between the symmetry axis and the line of sight). For any given radial coordinate at the funnel wall surface three possible cases are possible: the annulus is fully visible (this is possible only for $i < \theta_f$), invisible or partly visible. If the inclination is larger than θ_f for different radii either second or third case takes place for every annulus. Visibility may be quantitatively described by a factor y defined as the visible part of the given annulus (having constant distance r from the center). It may be determined by an analytical ray-tracing method.

$$\mathbf{r} = \mathbf{R} + s\mathbf{l}$$

Here \mathbf{l} is a unit vector directed towards the observer (we use the same scheme as in the previous section), \mathbf{R} is the radius vector of the intersection point between the funnel surface and the ray starting from \mathbf{r} and directed towards the observer. Boundary case when the intersection point

has the radial coordinate equal to the photosphere radius is of interest here. Normalizing over the outer radius ($x = r/r_{out}$), one can express the vectors as follows.

$$\begin{aligned}\mathbf{r} &= x \begin{pmatrix} \sin \theta_f \cos A \\ \sin \theta_f \sin A \\ \cos \theta_f \end{pmatrix} \\ \mathbf{R} &= \begin{pmatrix} \sin \theta_f \cos A_0 \\ \sin \theta_f \sin A_0 \\ \cos \theta_f \end{pmatrix} \\ \mathbf{l} &= \begin{pmatrix} \sin i \\ 0 \\ \cos i \end{pmatrix}\end{aligned}$$

It is easy to express two of the unknowns (s and A_0) from the others and obtain the solution for A (azimuthal coordinate of the starting point):

$$\sin A = \frac{1}{2} \left(\frac{\tan \theta_f}{\tan i} + \frac{\tan i}{\tan \theta_f} \right) + \frac{1}{2x} \left(\frac{\tan \theta_f}{\tan i} - \frac{\tan i}{\tan \theta_f} \right)$$

If the annulus is partially visible y may be calculated as the length of the arc (divided by 2π) connecting the two points defined by the solutions of the equation above. Finally:

$$y = \begin{cases} 0 & K < -1 \\ \frac{1}{2} + \frac{1}{\pi} \arcsin K & -1 \geq K > -1 \\ 1 & K \geq 1 \end{cases}, \quad (45)$$

where:

$$K = \frac{1}{2} \left(\frac{\tan \theta_f}{\tan i} + \frac{\tan i}{\tan \theta_f} \right) + \frac{1}{2x} \left(\frac{\tan \theta_f}{\tan i} - \frac{\tan i}{\tan \theta_f} \right)$$

4.2. Implications of Self-Occultation Effects

Watarai et al. (2005) studied self-occultation effects for fat accretion discs coming to an evident conclusion that the spectrum becomes softer at large inclinations. Heinzeller et al. (2007) comes to a similar conclusion considering the results of 2D RHD modelling by Ohsuga et al. (2005). In our case this effect is even more profound (see figure 6): at inclinations $i \sim \theta_f$ the X-ray component abruptly disappears (because only the inner parts of the funnel contribute significantly to the X-ray band) and only the EUV component may be observed.

Due to that reason some of SAs (those viewed at large inclinations) will not show the ULX phenomenon (see figure 7) but remain ULUVs (UltraLuminous UV sources). For $\theta_f = 0.4$ the number of “orphan” ULUVs is about $\cos \theta_f / (1 - \cos \theta_f) \sim 10$ times higher than the number of ULXs.

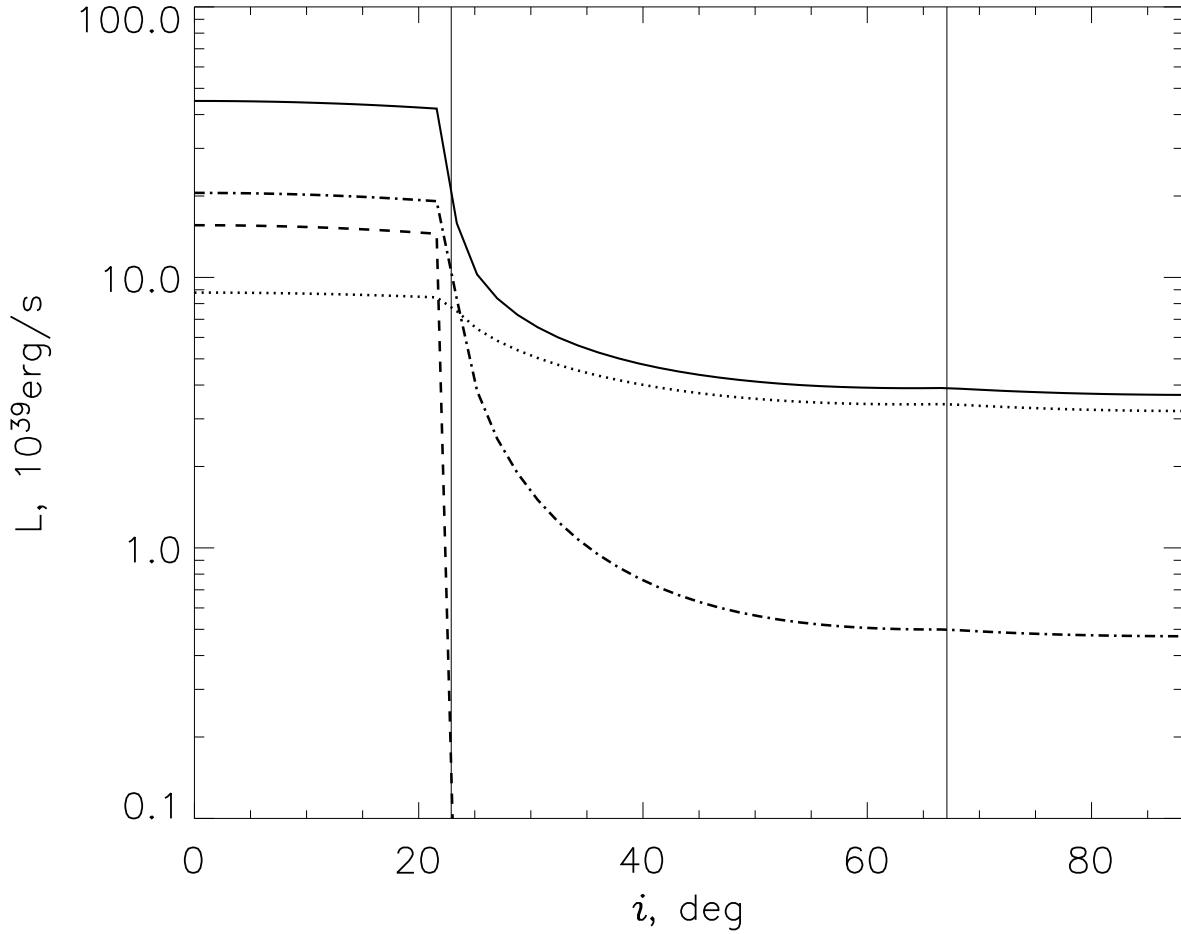


Fig. 6. Apparent isotropic luminosity as a function of inclination. Solid line represents bolometric luminosity. Dashed, dot-dashed and dotted lines represent harder X-rays ($0.4 \div 20$ keV), softer X-rays ($0.1 \div 0.4$ keV) and EUV ($0.01 \div 0.1$ keV). Vertical lines mark θ_f and $\pi/2 - \theta_f$.

Observations of these sources in the EUV are complicated by neutral gas absorption. In Abolmasov et al. (2008) we discuss the possibility of far-ultraviolet observations with *GALEX* (Martin et al. 2005). Supercritical accretors prove to be difficult but still reachable targets for *GALEX*, appropriate for pointing observations.

We do not know yet how much there is similarity between ULXs and SS433. SS433 exhibits jet/disc axis direction variations with a super-orbital precession period about 160^d. Similar effects are observed for some other X-ray binaries (Clarkson et al. 2003). There are indications that the supercritical disc (and consequently the wind with the funnel) follows the motions of the jets.

A nearly face-on SA may show periodical X-ray variability by one-two orders of magnitude when θ_f is less than the maximal and higher than the minimal value of i . Precessional

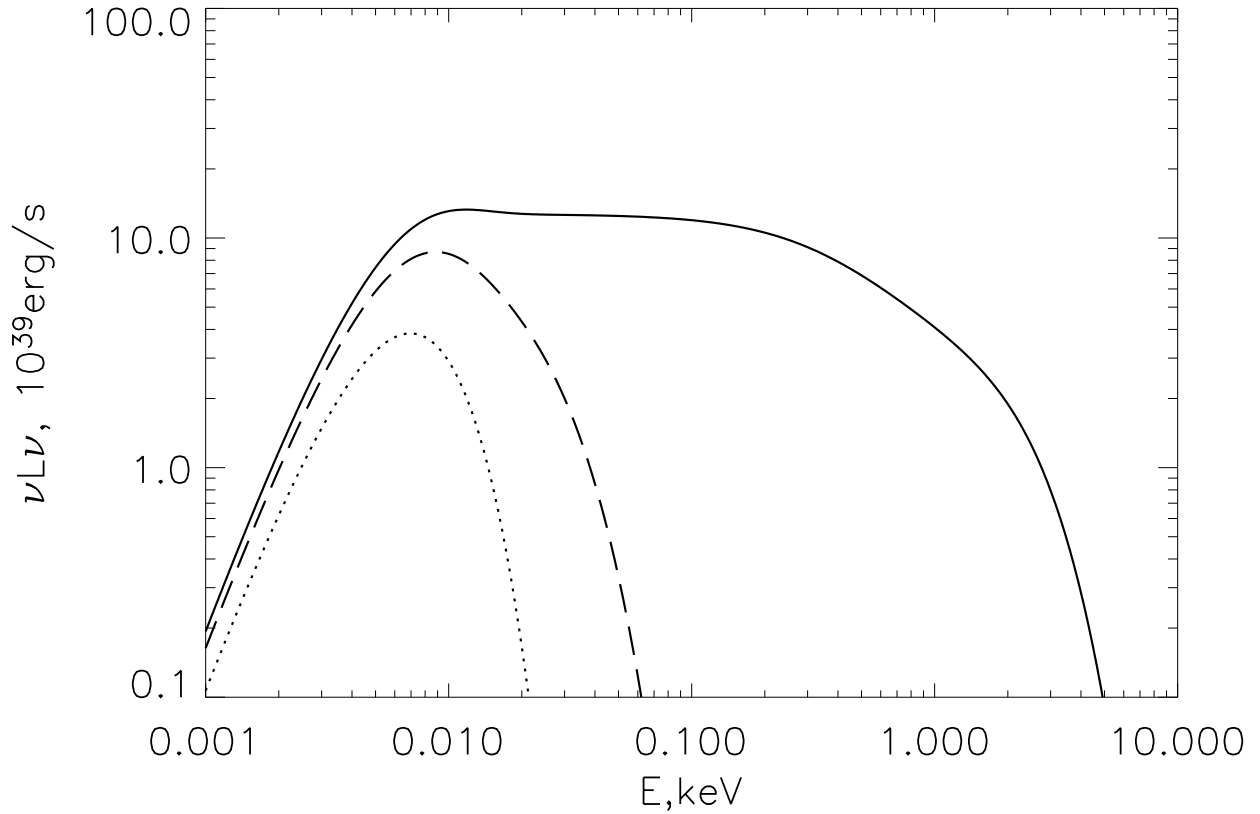


Fig. 7. Inclination effects on the outcoming spectra. Apparent values of νL_ν are shown for $i = 0, 25$, and 90 degrees as a solid, dashed and dotted lines, respectively. Higher apparent UV luminosity in the case of edge-on configuration is due to projection effects.

variability should have a distinguished light curve with a flat maximum and continuous flux change near the minimum light. In figure 8 we present the predicted X-ray spectra as functions of precessional phase for two sets of parameters. We assume here a simplified version of the kinematical model applied to SS433 (Abell & Margon 1979):

$$\cos i = \cos i_A \cos i_0 + \sin i_A \sin i_0 \cos(2\pi\psi),$$

where i_0 is the inclination with respect to the precession axis, i_A is the amplitude of inclination variation, and ψ is the phase of super-orbital period.

The only ULX exhibiting variability that may be considered super-orbital is X41.4+60 in M82 (Kaaret et al. 2006). *RXTE* X-ray flux varies by $\sim 50\%$ for this source with a 62^d period. Irregular variability on similar timescales is much more ordinary among ULXs (La Parola et al. 2001) possibly indicating that the funnel shape itself changes rapidly enough to level the effects of precessional variability.

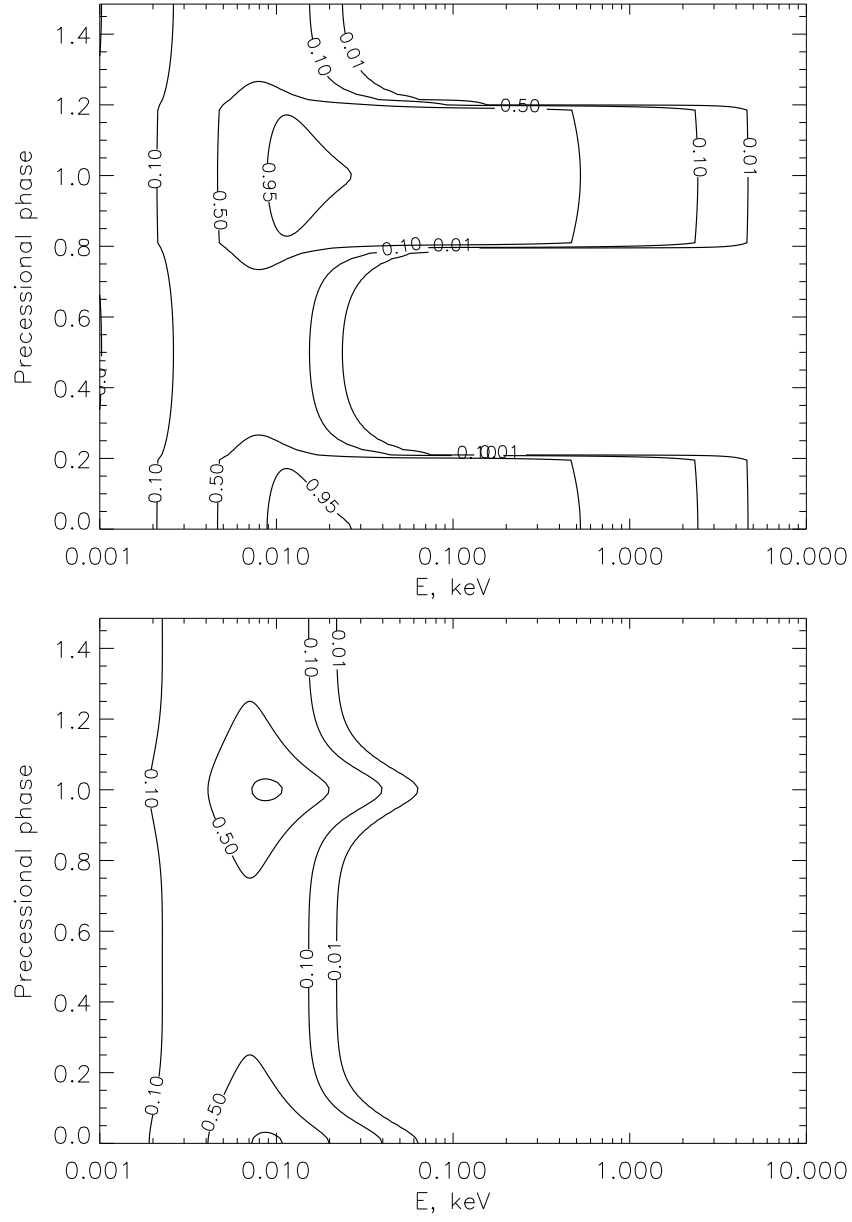


Fig. 8. Spectral variability of precessing SA. Lines of constant flux (EF_E) as a function of energy and precessional phase are given. Flux is normalized over its maximal value. $\theta_f = 22.9\text{deg}$, $\dot{m} = 10^3$, $\alpha = 0$. Upper diagram corresponds to $i_0 = 20\text{deg}$, lower to $i_A = 20\text{deg}$, lower has $i_0 = 45\text{deg}$ and $i_A = 20\text{deg}$. In the latter case funnel bottom is never visible and funnel walls remain at least partially occulted.

5. Comparison with Observations

5.1. Data on ULXs

XMM-Newton datasets on two X-ray sources, NGC4559 X-7 and NGC6946 ULX-1 were analysed. We used archive *XMM-Newton* EPIC MOS1,2 and PN (Turner et al. 2001) data obtained on 8 Oct 2006 (observation ID 0152170501) and 25 Jun 2004 (observation ID 0200670401), correspondingly. All the data were reduced using standard XMM SAS procedures. Response files were made using SAS tools `rmfgen` and `arfgen`. We set *flag*=0 for PN data. We used *pattern* ≤ 4 for PN and ≤ 12 for MOS data.

NGC4559 X-7 is known as a “supersoft” bright ULX (Cropper et al. 2004). It does not coincide with a bright stellar or nebular optical counterpart. However, there are indications that the source is connected with ~ 10 Myr old stellar population (Soria et al. 2005).

NGC6946 ULX1 (Roberts & Colbert 2003) is known to be a source of moderate luminosity $L_X \sim 3 \times 10^{39}$ ergs $^{-1}$ with an X-ray spectrum usual for ULXs. Stellar optical counterpart was detected by *HST* in the visible range (Blair et al. 2001) as a relatively bright star ($M_V \lesssim -7^m$). As many other ULXs, NGC6946 ULX1 coincides with a bright optical nebula. Abolmasov et al. (2008) analysing the emission spectrum of the nebula conclude that the central source may be a hard EUV source with temperature $T \sim 10^5$ K and luminosity $L \sim 10^{40}$ ergs $^{-1}$, roughly consistent with what one may expect from a $\dot{m} \sim 10^2$ SA.

Three models were used to fit the data: standard disc + power law (`diskbb+powerlaw`, Mitsuda et al. (1984)), p-free (`diskpbb`, Mineshige et al. (1994)) and self-irradiated multi-color funnel model (`sirf`) presented here. Efficiency of the p-free model for ULXs was already shown by Vierdayanti et al. (2006) and other works. Because the temperature of the funnel walls decays in a practically power-law manner (with $p \sim 0.5$ see figure 4) one should expect p-free model to give SEDs close to the SEDs predicted by our model. However, the temperature distribution required is very flat, so we have shifted the lowest allowed p from 0.5 to 0.05. For each object all the three extracted spectra were fitted simultaneously. Spectral ranges 0.1 – 12 keV for PN and 0.1 – 8 keV for MOS data were used.

In table 1 we present the results of fitting. It may be seen that in the case of NGC4559 X-7 two-component `diskbb+powerlaw` model gives the best results because of being capable to fit the harder part of the spectrum that is difficult to handle using only thermal models with exponential high-energy cut-offs.

`sirf` model requires low values of r_{in} and moderate accretion rates. $r_{in} \sim 10^{-3}$ is still reasonable for $\dot{m} \sim 100$. There is certain degeneracy between α and T_{in} , the latter being poorly constraint by itself because of limited spectral range and poor statistics at the hard end of the spectrum.

The well-known high-energy curvature (Dewangan et al. 2005) can be explained by $T_{in} \sim 0.5 \div 0.8$ keV. Best-fit α is higher for higher T_{in} making both virial ($\alpha \sim -0.5$) and

constant-velocity ($\alpha \sim 0$) laws acceptable. High inner temperatures like 10 keV also result in acceptable fits. Model is also insensitive to r_{out} save for the cases when this parameter is $\lesssim 1$.

Low values of best-fit θ_f for both sources may be a result of additional heating and hardening making the temperature slope flatter at $r \sim 1$. The same reason may be responsible for the low r_{out} values. Relativistic outflows and transversal velocity gradients may be responsible for this heating via shock waves and shear viscosity, correspondingly. On the other hand, the outflow may become inhomogeneous at about the spherisation radius (because the gas becomes cooling rapidly and therefore may become inhomogeneous). In this case the effective radius of the photosphere is lower and the temperature slope appears flatter, because higher surface area with $T \sim T(R_{sph})$ becomes visible. Porous winds may mimic winds with low θ funnels and lower \dot{m} . Another explanation is that comptonisation and reflection effects affect the outcoming spectrum making it harder (see next section).

Low values of r_{in} appear to be a real feature of ULXs. Funnel interior is expected to be practically transparent to the X-rays, probably having no “bottom photosphere”. Observations in a broader spectral range are needed to distinguish between the thermal radiation from the immediate vicinity of the compact object and comptonisation effects.

Though the model fits the data in a quite acceptable way its parameters are poorly constraint. The spectral shape does not depend very much on the actual accretion rate and velocity law. There are numerous ways of making the spectrum harder: taking into account the difference between mass accretion and ejection rates, applying comptonisation effects etc. All these effects will mostly affect the estimated mass accretion rate and r_{in} .

6. Discussion

6.1. Limitations of the Model

Our calculations do not account for radiation feedback on the dynamics. That is not only wind acceleration within the regions of interest but also evaporation from the funnel walls and development of instabilities in the outer parts of the funnel in the strong radiation field of the inner parts. The instability may resemble that of accretion discs with irradiation (see Mineshige (1993) and references therein) but the wind is unable to influence the irradiating source and its role in developing the instability is purely passive.

The structure of the inner parts of the flow may be much more complicated than we assumed. At $r \sim 1$ the source of the wind becomes spatially resolved and our radial approximation fails. Besides this, the angular distribution of the energy influx may be more complicated and higher angular harmonics may appear.

Qualitatively the effects of non-zero size mass loading region may be considered as follows: let us assume that $\dot{m} \propto r$. The main radial equation for $k = 0$ takes the form:

$$\partial_r u - \frac{1}{r^{2+\alpha}} \partial_r (r^{3+\alpha} \partial_r u) + \frac{\gamma(2+\alpha)}{r} u = 0$$

It is easy to check that the equation allows two power-law solutions ($u \propto r^\sigma$, where $\sigma = -0.5 \left((1+\alpha) \pm \sqrt{(1+\alpha)^2 + 4\gamma(2+\alpha)} \right)$) corresponding to inward and outward diffusion. For $r \ll 1$ and $\alpha = -0.5$ energy density decreases as $u \propto r^{-1.68}$ instead of $u \propto r^{-2}$. The difference increases for higher α .

We do not account for the emission of the hot interior of the funnel as well as for thermal comptonisation effects in the wind and pure reflection. All these effects are likely to harden the outcoming spectra making mass ejection rate estimates from the observational data shifted towards lower values. Hardening factor $T_h \simeq 2.6$ measured for standard discs (Borozdin et al. 1999) will lead to the mass ejection rate underestimate by a factor ~ 4 .

Reflection and absorption by moving partially ionized gas may simulate soft-excess observed in many ULX spectra (Stobbs et al. 2006) in a way it was proposed by Gierliński & Done (2004) for AGNi and recently by Gonçalves & Soria (2006) for ULXs. Understanding the structure of the outer photosphere of the wind requires more complicated modelling taking into account both significant non-sphericity of the outflow and various opacity sources.

6.2. Observational Predictions for ULXs

There are several effects expected if our estimates are correct: *(i)* supercritical accretors viewed at low inclinations ($i \lesssim \theta_f$) will be seen as ULXs ($L \gtrsim 10^{39}$ ergs $^{-1}$); *(ii)* independently of its inclination a supercritical accretor is an Ultra-Luminous UV source (ULUV); *(iii)* predicted X-ray spectra of supercritical accretors viewed face-on are similar to p-free model spectra with $p \sim 0.4 \div 0.6$; *(iv)* because of high EUV luminosities supercritical accretors should ionize the wind above the photosphere and establish Strömgren zones; *(v)* if the accretion disc precession characterising SS433 is usual for SAs viewed face-on strong X-ray flux modulation is expected for at least a number of sources with “super-orbital” periods like tens and hundreds of days.

Most of the observational properties of ULXs are naturally explained in our model. There is observational evidence that at least some ULXNe are powered by photoionisation from the central source having luminosity 10^{39} ergs $^{-1}$ or higher comparable with the X-ray luminosity. IMBH binaries should have difficulties in ionizing the surrounding gas unless the mass of the IMBH is very high, $\gtrsim 10^4 M_\odot$ (see discussion in Abolmasov et al. (2008)).

For very high accretion rates $\dot{m} \gtrsim 10^3$ the outer photosphere is very large comparable to the probable size of the binary system. Applying $\alpha = 0$ and $\theta_f = 0.4$ results in physical radius values:

$$R_{out} = 9 \times 10^{13} \dot{m}_3^{3/2} \text{ cm.} \quad (46)$$

However in a real high-mass binary conditions the structure of the outflow is perturbed by tidal forces and the outflowing gas itself rapidly recombines (see next section). Because the flow is essentially supersonic and perturbed by a strong non-axisymmetric potential it is likely

to become highly inhomogeneous. The equatorial outflow of SS433 is an example of such kind. The photosphere size in the optical then saturates at a radius of the order 10^{12}cm preventing SA from becoming “red hypergiants” with very high infrared luminosities. The effect may become significant starting from $\dot{m} \sim 100$.

Further understanding of SA winds will require methods used for stellar atmosphere calculations. Rosseland mean for $n \lesssim 10^{10}\text{cm}^{-3}$ and $T \sim 10^4 \div 10^5\text{K}$ is very close to κ_T (Iglesias & Rogers 1996) but in certain spectral ranges the wind should be less transparent. Edge-on ULX will mimic an OB-hypergiant with dense and fast wind or a low-temperature hydrogen-rich WR.

6.3. Photoionized Nebulae

In the case of highly supercritical accretion UV and EUV spectra may give much more information about the mass ejection rate than the X-ray properties. In figure 9 we show the dependence of H and He^+ -ionising fluxes ($1 \div 1.5$ and $4 \div 20\text{Ry}$ ranges, respectively) and corresponding luminosities of recombination emission lines on mass ejection rate. Here we suggest that the HII regions have fixed temperature $T = 10^4\text{K}$ and density $n = 100\text{cm}^{-3}$. Atomic data were taken from Osterbrock & Ferland (2006). One can see in the figure that high emission-line luminosities observed in ULXNe may be well explained by high EUV luminosities of the central sources. $\text{HeII}\lambda 4686 / \text{H}\beta$ ratios predicted in this model are close to the high $\text{HeII}\lambda 4686 / \text{H}\beta$ ratios ~ 0.2 measured for some high-excitation ULXNe or the inner high-excitation parts observed in some of the ULX shells (Abolmasov et al. 2007).

The situation becomes more complicated if one takes into account absorption in the wind optically thin to electron scattering. Density at the wind electron-scattering photosphere is

$$n = \frac{\dot{M}}{\Omega R_{out}^2 v} \simeq 10^8 \dot{m}_3^{-3/2} \text{cm}^{-3} \quad (47)$$

Recombination will occur in a layer having thickness:

$$\Delta R = \frac{v}{an} \simeq 10^{12} \dot{m}_3 M_{10} T_4^{-1/2} \text{cm}, \quad (48)$$

where $a \sim 10^{-13} T_4^{-1/2} \text{cm}^3 \text{s}^{-1}$ is the effective recombination rate and T_4 is gas temperature in 10^4K units. The size of the recombination region is close to or smaller than the size of the outer photosphere. Actually that means that the outer photosphere of the wind will be optically thick to the EUV radiation of the central source.

Hard radiation from the pseudo-photosphere may however ionize the gas. Because the density of the wind falls off rapidly two regimes appear: ionized and neutral wind. First case makes the photosphere of the wind a UV object with high bolometric correction and a compact HII-region coincident with the X-ray source. In the latter the photosphere is much cooler and mimicks a hypergiant with broad emission lines.

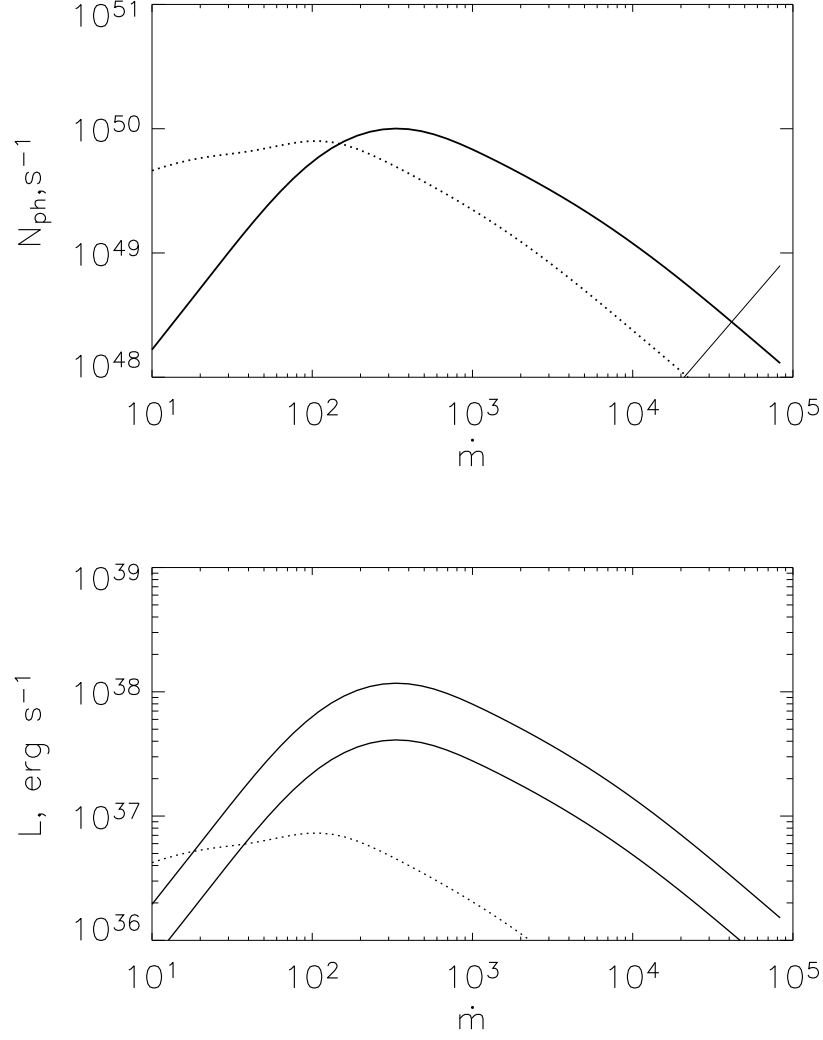


Fig. 9. Numbers of H (solid curve) and He^+ (dotted) -ionizing photons produced by the **sirf** model (upper panel) and the luminosities of relevant recombination lines (b): $\text{H}\alpha$ and $\text{H}\beta$ (solid) and $\text{HeII}\lambda 4686$ (dotted). $\alpha = 0$, $r_{\text{in}} = \dot{m}/6$ and $\theta_f = 23^\circ$ is assumed. Thin straight solid line marks the number of quanta absorbed in the wind.

The ability of the central source to ionize the wind may be calculated as follows. Recombination rate integrated over the outer wind is

$$I = \int_{R_{out}}^{R_{max}} a \Omega_f n^2(R) R^2 dR \quad (49)$$

R_{max} here is the radius of Strömngren zone ionized by the central source. I may be equated to the ionizing quanta production rate resulting in an equation:

$$S \simeq \frac{330GMa}{\sqrt{\cos\theta_f \Omega' \sigma_T^2 c^2}} \dot{m}^{3/2} \quad (50)$$

This recombination rate is usually lower than the quanta production rate affecting only the highest accretion rates. In figure 9 we present the ionizing quanta production rates for different mass ejection rates. ULX nebulae may appear even brighter due to two additional effects: “stripping” of the outer wind photosphere (the effect proposed in previous section) and higher accretion power due to $K < 1$.

7. Conclusions

Optically-thick wind with irradiation is capable to explain the SEDs of ULXs in the standard X-ray band and even the high-energy curvature that is difficult to explain in the framework of unsaturated comptonisation cool-disc IMBH model (Dewangan et al. 2005). High-energy cut-off is predicted to appear at several keV. Higher observed values of $T_{in} \sim 1 \div 3$ keV may be explained by applying a hardening factor $\sim 2 \div 3$ similar to those predicted for accretion discs in X-ray binaries.

Outcoming spectra observed at low inclinations are similar to the spectra of slim discs and resemble *p-free* model spectra with the *p* parameter near 0.5. X-ray spectra of known ULXs are well approximated by our model. However the parameters are poorly constraint supporting the idea that the properties of the X-ray spectrum depend rather weakly on the accretion parameters. Relatively high inner temperatures argue for the funnel interior to be transparent.

We stress the extreme importance of irradiation effects providing mild geometrical collimation of the observed X-ray radiation. In a simple assumption of local absorption and re-radiation of the absorbed energy we show that the temperature of the funnel wall surface is altered by about 20% at all the radii, and the outcoming apparent luminosity becomes about $2 \div 3$ times higher.

Our model suggests the outflow contains all the accreted mass (though the *Xspec* version easily accounts for any differences in the outflow and accretion rates). We also suggest the wind velocity close to the virial velocity at the spherisation radius. Due to that our results on the angular dependence of the outcoming spectrum differ from the results by Okuda (2002) and Heinzeller et al. (2007) and predict much softer spectra and much lower X-ray fluxes at high inclinations.

Photoionized nebulae are likely to be formed around SAs. Ionizing quanta production rates suggest that in most cases a SA is capable to produce a photoionized HII-region with optical emission line luminosities $\sim 10^{37}$ ergs $^{-1}$ but higher luminosities may appear as well.

The work was partially supported by the RFBR/JSPS grant 05-02-19710.

References

- Abell, G. O. & Margon, B. 1979, *Nature*, 279, 701
- Abolmasov, P., Fabrika, S., Sholukhova, O. & Afanasiev, V. 2007, *Astrophysical Bulletin*, 62, 36
- Abolmasov, P., Fabrika, S., Sholukhova, O. & Kotani, T. 2008, submitted to *PASJ*
- Abramowicz, M. A., Calvani, M. & Nobili, L. 1980, *ApJ*, 242, 772
- Abramowicz, M. A. 2004, Invited lecture at the conference “Growing Black Holes: Accretion in a Cosmological Context” (Garching, Germany, 21-25 June 2004) In print: “Growing Black Holes”, Eds. A. Merloni, S. Nayakshin and R. Sunyaev, “ESO Astrophysics Symposia Series”, Springer-Verlag, Berlin, 2004 ; astro-ph/0411185
- Bauer, F. E. & Brandt, W. N. 2004, *ApJL*, 601, 67
- Blair, W. P., Fesen, R. A. & Schlegel, E. M. 2001 *The Astronomical Journal*, 121, 1497
- Blundell, K. M., Mioduszewski, A. J. & Muxlow, T. W. B. 2001, *ApJL*, 562, 79
- Borozdin, K., Revnivtsev, M., Trudolyubov, S., Shröder, C. & Titarchuk, L. 1999, *ApJ*, 517, 367
- Clarkson, W. I., Charles, P. A., Coe, M. J., Laycock, S., Tout, M. D. & Wilson, C. A. 2002, *MNRAS*, 339, 447
- Cropper, M., Soria, R., Mushotzky, R. F., Wu, K. Markwardt, C. B. & Pakull, M. 2004, *MNRAS*, 353, 1024
- Dewangan, G. C., Griffiths, R. E. & Rao, A. R. 2005, astro-ph/05111102
- Dolan J. F., Boyd P. T., Fabrika S. et al. 1997 *A&A*, 327, 648
- Dwight, H. B. 1961, “Tables of Integrals”, New York: the MacMillan Company
- Eggum, G.E., Coroniti, F.V. & Katz, J.I. 1985, *ApJ*, 330, 142
- Fabbianom G., 1989, *ARA&A*, 27, 87
- Fabrika, S. “Supercritical disk and jets of SS433” 2004, *ASPR*, vol. 12
- Frank, J., King, A. & Raine, D. 2002, “Accretion Power in Astrophysics”, Cambridge: Cambridge University Press, third edition
- Fryer, C. L. & Kalogera, V. 2001, *ApJ*, 554, 548
- Gierliński, M. & Done, C. 2004, *MNRAS Letters*, 349, 7
- Gonçalves, A. C. & Soria, R. 2006, *MNRAS Letters*, 371, 673
- Goranskii, V. P., Esipov, V. F. & Cherepashchuk, A. M. 1998, *Astronomy Reports*, 42, 209
- Heinzeller, D., Mineshige, S. & Ohsuga, K. 2007, *MNRAS*, 372, 1208
- Van den Heuvel, E. P. J. 1981, *Vistas in Astronomy*, 25, 95
- Iglesias, C. A. & Rogers, F. G. 1996, *ApJ* 464, 943
- E. Jahnke and F. Emde (revised by F. Lsch), “Tables of Higher Functions” (McGraw-Hill, New York, 1960).

- Kaaret, P., Simet, M. G. & Lang, C. C. 2006, *ApJ*, 646, 174
- Katz, J. 1986, *Comments Astrophys.*, 11, 201
- Kobulnicky, H. A. & Fryer, C. L. 2007, *ApJ*, 670, 747
- Lucy, L. B. 2008, *astro-ph/0607225*
- Martin, C. et al., 2005, *ApJ*, 619, 1L
- Mineshige, S. 1993, *Astrophysics and Space Science*, 210, 83
- Mineshige, S., Hirano, A., Kitamoto, S., Yamada, T. & Fukue, J. 1994, *ApJ*, 426, 308
- Mitsuda, K., Inoue, H., Koyama, K. et al. 1984, *PASJ*, 36, 741
- Ohsuga, K., Mori, M., Nakamoto, T. & Mineshige, S. 2005, *ApJ*, 628, 368
- Okuda T. 2002, *PASJ*, 54, 253
- Osterbrock, D. E. & Ferland, G. “Astrophysics of Gaseous Nebulae and Active Galactic Nuclei” 2006, 2nd. ed. by D.E. Osterbrock and G.J. Ferland. Sausalito, CA: University Science Books, 2006
- La Parola, V., Peres, G., Fabbiano, G., Kim, D. W. & Bocchino, F. 2001, *ApJL*, 556, 47
- Poutanen, J., Lipunova, G., Fabrika, S., Butkevich, A. & Abolmasov, P. 2007, *MNRAS*, 377, 1187
- Roberts, T. P. 2007, *astro-ph/0706.2562*
- Roberts, T. P. & Colbert, E. J. M. 2003, *MNRAS*, 341, 49
- Roberts, T. P., Goad, M. R., Ward, M. J. & Warwick, R. S. 2003, *MNRAS*, 342, 709
- Shakura, N. I. & Sunyaev, R. A. 1973, *A&A*, 24, 337
- Shklovskii, I.S. 1981, *Sov. Astron.* 25, 315
- Soria, R., Cropper, M., Pakull, M., Mushotzky, R. & Wu, K. 2005, *MNRAS*, 356, 12
- Stobbart, A.-M., Roberts, T. P. & Wilms, J. 2006, *mNRAS*, 368, 397
- Turner, M. J. L., Abbey, A., Arnaud, M., et al. 2001, *A&AL*, 365, 27
- Vierdayanti, K., Mineshige, S., Ebisawa, K. & Kawaguchi, T. 2006, *PASJ*, 58, 915
- Watarai, K.-y., Ohsuga, K., Takahashi, R. & Fukue, J. 2005, *PASJ*, 57, 513

Table 1. Best fitting results for the two selected ULXs. Errors correspond to 90% confidence range.

	NGC4559 X-7	NGC6946 ULX-1
phabs(diskbb + powerlaw)		
$N_H, 10^{22} \text{ cm}^{-2}$	$0.219^{+0.03}_{-0.02}$	$0.44^{+0.08}_{-0.05}$
$T_{in}, \text{ keV}$	$0.155^{+0.010}_{-0.009}$	$0.156^{+0.018}_{-0.019}$
$diskbbnorm$	150^{+120}_{-60}	620^{+2000}_{-200}
Γ	$2.24^{+0.05}_{-0.05}$	$2.46^{+0.15}_{-0.09}$
$powerlawnorm$	$2.3^{+0.14}_{-0.14} \times 10^{-4}$	$3.3^{+0.6}_{-0.5} \times 10^{-4}$
χ^2/DOF	648/673	523/504
$L_{model}, 10^{39} \text{ erg s}^{-1}$	$9.6^{+0.4}_{-1.6}$	$3.1^{+3}_{-1.0}$
phabs(diskpbb)		
$N_H, 10^{22} \text{ cm}^{-2}$	$0.0407^{+0.0011}_{-0.0009}$	$0.293^{+0.03}_{-0.016}$
$T_{in}, \text{ keV}$	$0.64^{+0.22}_{-0.23}$	$2.3^{+0.4}_{-0.4}$
p	$0.460^{+0.004}_{-0.005}$	$0.404^{+0.01}_{-0.01}$
$diskpbbnorm$	$1.4^{+0.9}_{-0.5} \times 10^{-4}$	$3.3^{+2}_{-0.4} \times 10^{-4}$
χ^2/DOF	734/674	665/509
$L_{model}, 10^{39} \text{ erg s}^{-1}$	9^{+6}_{-3}	3 ± 1
phabs(sirf)		
$N_H, 10^{22} \text{ cm}^{-2}$	$0.12^{+0.03}_{-0.04}$	$0.26^{+0.04}_{-0.02}$
$T_{in}, \text{ keV}$	$1^{+0.5}_{-0.2}$	$0.85^{+0.2}_{-0.15}$
r_{in}	$0.00126^{+0.0006}_{-0.0011}$	$0.016^{+0.017}_{-0.011}$
r_{out}	60^{+119}_{-5}	$2.4^{+1.6}_{-0.7}$
θ	8^{+4}_{-3}	$5.8^{+0.3}_{-0.3}$
α	$-0.5^{+0.4}_{-0.15}$	$-0.4^{+0.4}_{-0.2}$
$norm$	13^{+9}_{-6}	$2.4^{+0.4}_{-0.18}$
χ^2/DOF	614/671	510/502
$L_{model}, 10^{39} \text{ erg s}^{-1}$	9.6^{+6}_{-4}	3^{+2}_{-1}

Appendix 1. Integration over φ

The integral over φ can be calculated as follows:

$$I = R^2 \int_{-\pi}^{\pi} w(R'/R, \theta_f, \varphi) d\varphi = \frac{1}{2\pi} x \sin^2 \theta_f \cos^2 \theta_f \int_{-\pi}^{\pi} \frac{(1 - \cos \varphi)^2}{(a + b \cos \varphi)^2} d\varphi$$

Where $a = 1 - 2x \cos^2 \theta_f + x^2$, $b = -2x \sin^2 \theta_f$.

$$\begin{aligned} I &= \frac{1}{2\pi} x \sin^2 \theta_f \cos^2 \theta_f \left(\int_{-\pi}^{\pi} \frac{1}{(a + b \cos \theta_f)^2} d\varphi - 2 \int_{-\pi}^{\pi} \frac{\cos \varphi}{(a + b \cos \theta_f)^2} d\varphi + \int_{-\pi}^{\pi} \frac{\cos^2 \varphi}{(a + b \cos \theta_f)^2} d\varphi \right) = \\ &= \frac{1}{2\pi} x \sin^2 \theta_f \cos^2 \theta_f \left(\left(1 - \frac{a^2}{b^2}\right) \int_{-\pi}^{\pi} \frac{1}{(a + b \cos \theta_f)^2} d\varphi - 2 \left(1 + \frac{a}{b}\right) \int_{-\pi}^{\pi} \frac{\cos \varphi}{(a + b \cos \theta_f)^2} d\varphi + \frac{2\pi}{b^2} \right) \end{aligned}$$

The two integrals can be expressed as follows (for details see for example Dwight 1961 or any other table of integrals):

$$\begin{aligned} \int_{-\pi}^{\pi} \frac{1}{(a + b \cos \theta_f)^2} d\varphi &= \frac{a}{(a^2 - b^2)} \int_{-\pi}^{\pi} \frac{1}{a + b \cos \theta_f} d\varphi = \frac{2\pi a}{(a^2 - b^2)^{3/2}} \\ \int_{-\pi}^{\pi} \frac{\cos \varphi}{(a + b \cos \theta_f)^2} d\varphi &= -\frac{b}{a^2 - b^2} \int_{-\pi}^{\pi} \frac{1}{a + b \cos \theta_f} d\varphi = -\frac{2\pi b}{(a^2 - b^2)^{3/2}} \end{aligned}$$

Finally, the integral value becomes:

$$I = \frac{x \sin^2 \theta_f \cos^2 \theta_f}{b^2} \left(1 - \sqrt{\frac{a+b}{a-b}} \frac{a-2b}{a-b} \right) = \frac{2\pi x \cot^2 \theta_f}{4} \left(1 - \frac{|1-x|}{\sqrt{1-2x \cos(2\theta_f) + x^2}} \frac{1-2x(1-3\sin^2 \theta_f) + x^2}{1-2x \cos(2\theta_f) + x^2} \right)$$